Spiro-based thermally activated delayed fluorescence emitters with reduced non-radiative decay for high quantum efficiency, low roll-off, light-emitting diodes

Nidhi Sharma[‡a,b], Michal Maciejczyk[‡c], David Hall[b,d], Wenbo Li[a], Vincent Liégeois[f], David Beljonne[d]*, Yoann Olivier[d,e]*, Neil Robertson[c]*, Ifor D. W. Samuel[a]* and Eli Zysman-Colman[b]*

[a] Organic Semiconductor Centre, SUPA, School of Physics and Astronomy, University of St Andrews, North Haugh, St Andrews, KY16 9SS, U.K. E-mail: idws@st-andrews.ac.uk

[b] Organic Semiconductor Centre, EaStCHEM School of Chemistry, University of St Andrews, St Andrews, Fife, KY16 9ST, UK. E-mail: eli.zysman-colman@st-andrews.ac.uk ; Web: http://www.zysman-colman.com; Fax:+44 (0)1334 463808; Tel:+44 (0)1334 463826.

[c] EaStCHEM School of Chemistry, University of Edinburgh

King's Buildings, Edinburgh EH9 3FJ, UK E-mail: neil.robertson@ed.ac.uk

[d] Laboratory for Chemistry of Novel Materials, University of Mons, Place du Parc 20, B-7000 Mons, Belgium.

[e] Unité de Chimie Physique Théorique et Structurale & Laboratoire de Physique du Solide, Namur Institute of Structured Matter (NISM), Université de Namur, Rue de Bruxelles, 61, 5000 Namur, Belgium.

[f] Unité de Chimie Physique Théorique et Structurale, Namur Institute of Structured Matter (NISM), Université de Namur, Rue de Bruxelles, 61, 5000 Namur, Belgium.

[‡] contributed equally

Abstract

Herein, we report the use of spiro-configured fluorene-xanthene scaffolds as a novel, promising and effective strategy in thermally activated delayed fluorescence (TADF) emitter design to attain high photoluminescence quantum yields (Φ_{PL}), short delayed luminescence lifetime, high external quantum

efficiency (EQE) and minimum efficiency roll-off characteristics in organic light-emitting diodes (OLEDs). The optoelectronic and electroluminescence properties of **SFX-**, spiro-(fluorene-9,9'-xanthene), based emitters (**SFX-PO-DPA, SFX-PO-DPA-Me** and **SFX-PO-DPA-OMe**) were investigated both theoretically and experimentally. All three emitters exhibited sky blue to green emission enabled by a Herzberg-Teller mechanism in the excited state. They possess short excited state delayed lifetimes (<10 μs), high photoluminescence quantum yields (Φ_{PL} ~70%) and small singlet-triplet splitting energies (ΔE_{ST} < 0.10 eV) in the doped films in an mCP host matrix. The OLEDs showed some of the highest EQEs using spiro-containing emitters where maximum external quantum efficiencies (EQE_{max}) of 11% and 16% were obtained for devices using **SFX-PO-DPA** and **SFX-PO-DPA-OMe**, respectively. Further, a record EQE_{max} of 23% for a spiro-based emitter coupled with a small efficiency roll off (19% at 100 cd m^{-2}) was attained with **SFX-PO-DPA-Me.**

Introduction.

Thermally activated delayed fluorescence (TADF) has emerged as a very popular mechanism for harvesting excitons in organic light-emitting diodes (OLEDs).[1-3] Metal-free TADF materials, like state-of-the-art phosphorescent materials, can harvest 100% of the generated excitons and convert them into light. Electroluminescent devices using TADF emitters exhibit comparable efficiencies to state-of-the-art phosphorescent OLEDs. An efficient TADF mechanism is observed from charge transfer (CT) systems that possess a small singlet-triplet energy gap (ΔE_{ST}) as a consequence of the small exchange integral. In donor-acceptor TADF emitter architectures, hole and electron densities in the lowest singlet and triplet excited states are spatially separated. This is frequently due to a large torsion between donor and acceptor fragments. A small ΔE_{ST} allows for efficient reverse intersystem crossing (RISC), resulting in an observed TADF upon photo- or electrical excitation. However, unlike phosphorescent OLEDs, TADF OLEDs frequently suffer from high efficiency roll-off at high current densities due to the relatively longer delayed exciton lifetimes (τ_d) of the emitters.[4] Many efforts have been devoted to combat this limitation by incorporating a properly designed TADF emitter.[5-7] For example, it has already been established both theoretically and experimentally that a highly twisted donor-acceptor

structure with a correspondingly small ΔE_{ST} is desired to achieve high RISC rates.[8-9] However, this approach leads to low oscillator strength, and the resulting low radiative decay rate of the emissive S_1 state usually lead to low photoluminescence quantum yields, Φ_{PL}. There is, therefore, a challenge in emitter design to conceive of a system that possesses both small ΔE_{ST} and high Φ_{PL} in order to realize efficient TADF OLEDs.

Very small ΔE_{ST} values can be easily obtained in spiro-type compounds where donor and acceptor moieties are disposed orthogonally with respect to each other. Owing to their three-dimensional structure, excimer emission is suppressed in the solid state. Spiro compounds also possess excellent thermal stability, high glass transition temperatures, and have been widely studied as optoelectronic materials.[10-15] Despite having such favourable structural, thermal and optoelectronic properties that would make them highly suited as TADF emitters, there have been only a handful of reports of emitter design based on spiro architectures. Figure **1** shows all reported spiro-based TADF emitters. The first example of a spiro-based TADF compound, **spiro-CN**,[16] is a yellow-emitting material (λ_{PL} = 545 nm) with a ΔE_{ST} and τ_d of 0.056 eV and 14 μs, respectively, in 6 wt% mCP doped films. The Φ_{PL}, however, remained only 27% and the resulting OLEDs displayed a maximum external quantum efficiency, EQE_{max}, of only 4.4% with λ_{EL} of 550 nm. Upon incorporation of the donor fragment within the spiro framework as in **ACRFLCN**,[17] the photophysical properties and the device performances were improved significantly. **ACRFLCN** exhibited sky blue emission (λ_{PL} = 485 nm) with a vanishingly small ΔE_{ST} of 0.01 eV but with a rather long τ_d of 3.9 ms in 6 wt % doped TPSI-F films. The Φ_{PL} in the solid state was nearly 67% and the OLEDs possessed an improved EQE_{max} of 10.1% with λ_{EL} = 500 nm; however, the devices showed rather high efficiency roll-off. When both the donor and acceptor units are intrinsically a part the spiro framework as in **ACRSA**,[18] sky blue emission was obtained (λ_{PL} = 490 nm). In the 20 wt% DPEPO doped films, a small ΔE_{ST} of 0.030 eV, short τ_d of 5.3 μs and high Φ_{PL} of 81% were obtained. The resulting OLEDs showed a much-improved EQE_{max} of 16.5% with a λ_{EL} of 490 nm. However, this high EQE_{max} was obtained at a very low current density of 0.01 mA cm^{-2}. The emitter **DPAA-AF**,[19] where the acridine core donor unit is substituted with

peripheral electron-donating diphenylamines, exhibited blue-green emission (λ_{PL} = 490 nm), a ΔE_{ST} of 0.021 eV, τ_d of 4.3 μs and Φ_{PL} of 70% in 6 wt% mCP doped films. The OLEDs showed an EQE_{max} of 9.6% and an λ_{EL} of 499 nm. Two emitters **OSTFCN** and **OSTFB** were reported[20] based on a modified design of the emitter **ACRSA**. **OSTFCN** and **OSTFB** both showed green-yellow emission with λ_{PL} of 530 and 550 nm, accompanied by relatively larger ΔE_{ST} of 90 and 0.110 eV, longer τ_d of 150 and 180 μs and Φ_{PL} of 80% and 60%, respectively, in 10 wt% mCP doped films. The OLEDs displayed high EQE_{max} values of 20.4% and 18.8% with λ_{EL} of 530 and 550 nm for **OSTFCN** and **OSTFB**, respectively. The spiro-blocking strategy has recently been demonstrated to realize deep blue TADF emission in non-doped devices of the emitter **TXADO spiro DMACF**.[21] This emitter possessed a λ_{PL} of 445 nm, a Φ_{PL} of 54%, a much larger ΔE_{ST} of 0.280 eV resulting in a longer τ_d of 160 μs in neat films. Non-doped OLEDs based on **TXADO spiro DMACF** showed deep blue emission [λ_{EL} = 444 nm; CIE of (0.16, 0.09)]. However, the EQE_{max} of the OLED was limited to 5.3% and device suffered from severe efficiency roll-off at high current densities. Recently, emitter **SAF-3CN**, a slightly modified design of **ACRFLCN** was reported,[22] where an additional electron-withdrawing cyano group was introduced at the C4 site of the fluorene moiety (Figure **1**). **SAF-3CN** showed green emission with λ_{PL} of 540 nm, Φ_{PL} of 65%, a small ΔE_{ST} of 0.01 eV and τ_d of 21.5μs in 2 wt% doped films in CBP host. The OLEDs exhibited green emission [λ_{EL} = 532 nm; CIE of (0.36, 0.57)] and an EQE_{max} of 19.4%, which reduced to 14.4% at 1000 cd m^{-2}. The **ACRFLCN** moiety was modified in emitter **QAFCN** to generate a more rigid donor structure in order to enhance both the Φ_{PL} and RISC in the solid state.[23] **QAFCN** showed sky-blue emission with λ_{PL} = 490 nm, Φ_{PL} of 71%, and ΔE_{ST} of 0.19 eV in 12 wt% doped films in DPEPO host. The resulting sky-blue OLEDs [λ_{EL} = 488 nm; CIE of (0.19, 0.35)] showed an EQE_{max} of 17.9%, which reduced significantly to 9.5% at high current density of 100 cd m^{-2}. From this analysis, it is evident that spiro-configured architectures incorporated into the emitter design beneficially contribute towards small ΔE_{ST} values; however, to concurrently maintain a high Φ_{PL} and a short τ_d for this class of emitter remains a major challenge.

Spiro-CN
λ_{PL} = 545 nm, ΔE_{ST} = 0.056 eV, τ_d = 14 μs, Φ_{PL} = 27% ; 6 wt% mCP film
λ_{EL} = 550 nm, EQE_{max} = 4.4%, CIE N/A
Chem. Commun. **2012**, 48, 9580.

ACRFLCN
λ_{PL} = 485 nm, ΔE_{ST} = 0.01 eV, τ_d = 3.9 ms, Φ_{PL} = 67% ; 6 wt% TPSi-F film
λ_{EL} = 500 nm, EQE_{max} = 10.1%, CIE N/A
Angew. Chem. Int. Ed. **2012**, 51, 11311.

ACRSA
λ_{PL} = 490 nm, ΔE_{ST} = 0.03 eV, τ_d = 5.3 μs, Φ_{PL} = 81% ; 20 wt% DPEPO film
λ_{EL} = 490 nm, EQE_{max} = 16.5%, CIE N/A
Chem. Commun. **2013**, 49, 10385.

DPAA-AF
λ_{PL} = 490 nm, ΔE_{ST} = 0.021 eV, τ_d = 4.3 μs, Φ_{PL} = 70% ; 6 wt% mCP film
λ_{EL} = 499 nm, EQE_{max} = 9.6%, CIE N/A
Chem. Lett. **2014**, 43, 1017

OSTFCN
λ_{PL} = 530 nm, ΔE_{ST} = 0.09 eV, τ_d = 150 μs, Φ_{PL} = 80% ; 10 wt% mCP film
λ_{EL} = 530 nm, EQE_{max} = 20.4%, CIE N/A
Org. Lett. **2017**, 19, 3155.

OSTFB
λ_{PL} = 550 nm, ΔE_{ST} = 0.11 eV, τ_d = 180 μs, Φ_{PL} = 60% ; 10 wt% mCP film
λ_{EL} = 550 nm, EQE_{max} = 18.8%, CIE N/A
Org. Lett. **2017**, 19, 3155.

TXADO spiro DMACF
λ_{PL} = 445 nm, ΔE_{ST} = 0.28 eV, τ_d = 160 μs, Φ_{PL} = 54% ; Neat film
λ_{EL} = 444 nm, EQE_{max} = 5.3%, EQE_{100} = 3.0%, CIE = (0.16, 0.09)
ACS Omega **2019**, 4, 1861.

SAF-3CN
λ_{PL} = 540 nm, ΔE_{ST} = 0.01 eV, τ_d = 21.5 μs, Φ_{PL} = 65% ; 2 wt% CBP film
λ_{EL} = 532 nm, EQE_{max} = 19.4%, CIE (0.36, 0.57)
J. Mater. Chem. C. **2020**, 8, 8579

QAFCN
λ_{PL} = 490 nm, ΔE_{ST} = 0.19 eV, Φ_{PL} = 71% ; 12 wt% DPEPO film
λ_{EL} = 488 nm, EQE_{max} = 17.9%, CIE (0.19, 0.35)
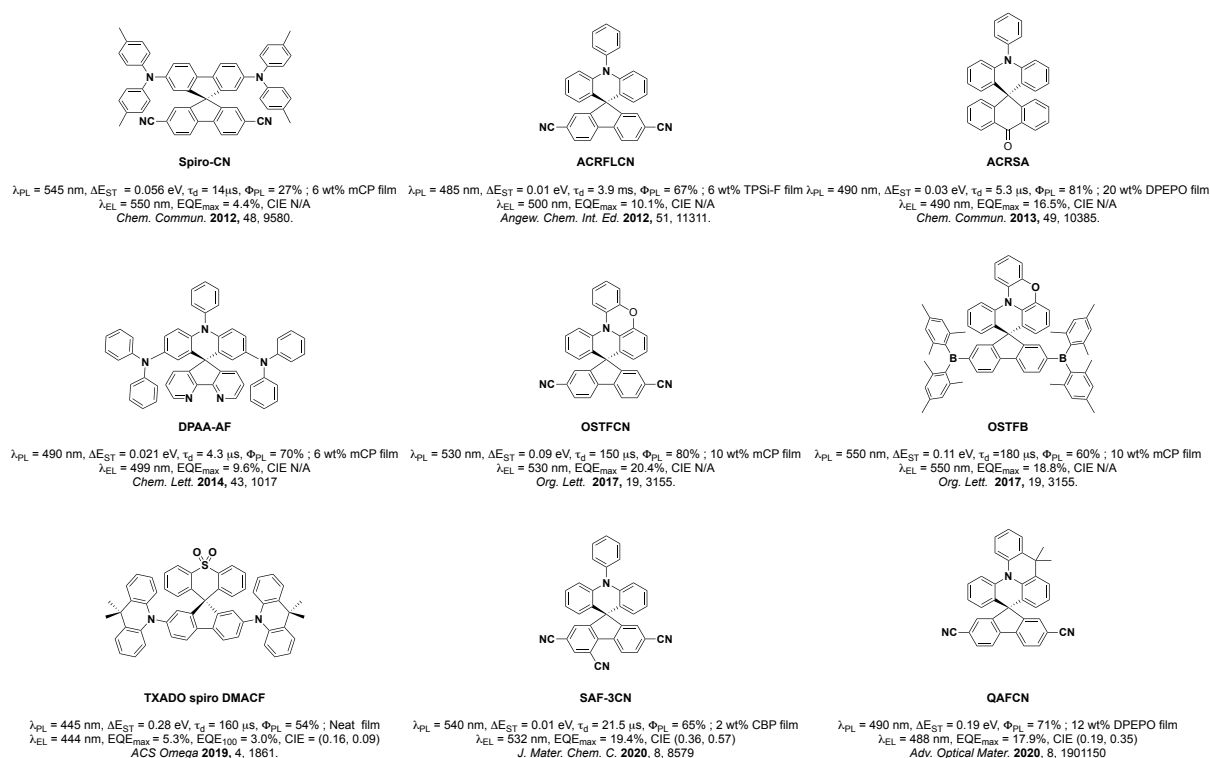*Adv. Optical Mater.* **2020**, 8, 1901150

Figure **1**. Chemical Structures and performances of literature spiro-based TADF compounds.

From the synthetic point of view all the previously reported structures are very similar since they have either non-aromatic acceptor as with nitriles (**Spiro-CN**, **ACRFLCN, OSTFCN, SAF-3CN and QAFCN**) or the acceptor substituent is incorporated into one of the spiro π-systems (**ACRSA**, **OSTFB**, **DPAA-AF** and **TXADO spiro DMACF**). This may simplify, in some cases, the synthesis of these materials but it also restricts molecular design to a small number of donor-acceptor pairs, thereby limiting the utilization of the great potential associated with the spiro architecture for designing highly efficient TADF emitters.

We report here a promising molecular design strategy to concurrently obtain a small $\Delta E_{ST,}$ high Φ_{PL}, short τ_d in TADF emitters that should translate to OLEDs with high EQEs and improved efficiency roll-off. We developed three highly efficient TADF emitters by incorporating an **SFX**, spiro-(fluorene-9,9'-xanthene), system[24] where a fluorene unit decorated with weakly electron-accepting phosphine

oxides is spiro-linked to a xanthene core containing pendant diarylamine donors (Figure **2**). As with most of the spiro compounds, our **SFX**-based emitters exhibit very weak spatial overlap between the frontier molecular orbitals due to the mutually orthogonal donor (D) and acceptor (A) orientation, so that the lowest electronic excitation should be 'dark'. However, vibronic coupling in the lowest excited state can result in intensity borrowing from higher-lying bright states, imparting the emissive state with non-negligible oscillator strength and radiative decay rates.

The presented materials and synthetic approach circumvent current spiro-based molecular design limitations by exploiting electronic separation of unsubstituted fluorene and xanthene π-systems thus facilitating easy, stepwise introduction of aromatic acceptors on one half, followed by bromination of the other half that then permits facile introduction of the aromatic donors. We tuned the degree of overlap between HOMO and LUMO moieties through the choice of donor system in order to achieve efficient radiative decay and short τ_d while maintaining a small ΔE_{ST}. Further, the inherent rigidity of a spiro centre also restricts both intramolecular non-radiative decay to the ground state from either the first singlet (S_1) or triplet (T_1) excited states and intermolecular interactions in the solid state, which limits bimolecular recombination processes such as triplet-triplet and triplet-polaron annihilations, contributing to the high Φ_{PL}. Three novel emitters, **SFX-PO-DPA, SFX-PO-DPA-Me** and **SFX-PO-DPA-OMe** were synthesized, and their optoelectronic properties were investigated and corroborated by a thorough computational study. All three TADF emitters showed short τ_d (<10 μs), high Φ_{PL} (~70%) and modest ΔE_{ST} (ca. 0.10 eV) in doped films in a mCP host matrix. The OLEDs incorporating these emitters exhibited sky-blue to green emission. EQE_{max} values approaching 11% and 16% were obtained for **SFX-PO-DPA** and **SFX-PO-DPA-OMe**, respectively. Impressively, the OLED with **SFX-PO-DPA-Me** as the emitter showed an EQE_{max} of 23% combined with low efficiency roll-off (EQE_{100} = 19% at 100 cd m^{-2}). This device performance validates the SFX spiro design and places it as the most efficient OLED among those employing spiro-configured TADF emitters to date.
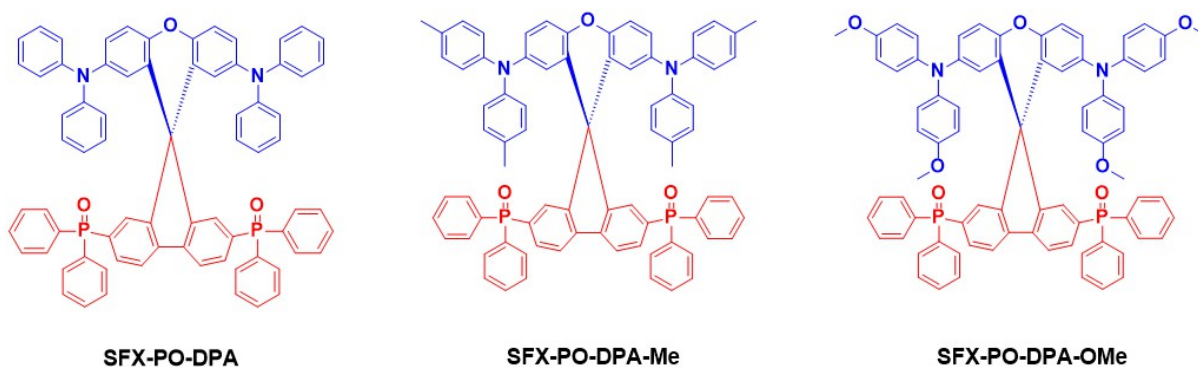
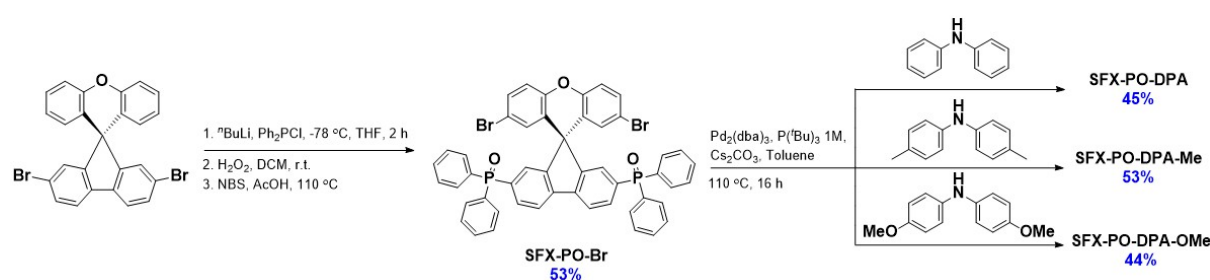Figure **2**. Chemical Structures of **SFX-PO-DPA**, **SFX-PO-DPA-Me and SFX-PO-DPA-OMe**.

Results and Discussion

Synthesis

The synthetic procedures for the preparation of SFX-based emitters are presented in Scheme **1**. The starting material, 2,7-dibromospiro[fluorene-9,9'-xanthene] **SFX-Br** was prepared according to a modified protocol[25] reported for the large-scale synthesis of spiro[fluorene-9,9'-xanthene].[26] Spiro[fluorene-9,9'-xanthene]-2,7-diylbis(diphenylphosphine oxide) **SFX-PO** was synthesized according to the literature.[27] The selective electrophilic aromatic dibromination of the xanthene ring of the **SFX-PO** scaffold was achieved by utilization of *N*-bromosuccinimide (NBS) in glacial acetic acid at elevated temperature (110 ºC) in a good yield of 72%; room temperature reaction in glacial acetic acid and acetonitrile gave only starting material. The successful conditions left the deactivated fluorene and diphenylphosphine oxide rings untouched by taking advantage of electronic separation from the more reactive xanthene half, even in the presence of excess (4 equiv.) NBS. The total yield after three steps for this **SFX-PO-Br** intermediate was 53%. The emitters were obtained by Buchwald-Hartwig coupling of **SFX-PO-Br** and three different diphenylamines: diphenylamine, 4,4'-dimethyldiphenylamine and 4,4'-dimethoxydiphenylamine. Three different combinations of catalyst, base and ligand were evaluated: Pd$_2$(dba)$_3$, P(*t*-Bu)$_3$ and NaO*t*-Bu in toluene at 110 ºC for 16 h gave a mixture of products. Pd(OAc)$_2$, [(*t*-Bu)$_3$PH]BF$_4$ and NaO*t*-Bu in toluene at 110 ºC for 16 h gave only starting materials. However, utilization of cesium carbonate as a base with Pd$_2$(dba)$_3$ as the catalyst and P(*t*-Bu)$_3$ as the ligand successfully yielded the desired products with moderate yields of 45%, 53%, 44% for **SFX-PO-DPA**, **SFX-PO-DPA-Me** and **SFX-PO-DPA-OMe**, respectively. As has been previously

reported, the use of a weaker base like cesium carbonate provides better compatibility with base-sensitive functional groups.[28]

This approach permits tuning of the optoelectronic properties of the emitters by appropriate choice of donor-acceptor combinations. Here, we tested only diphenylphosphine oxide as an acceptor and focused on the influence on the different diphenylamine substituents. However, the results indicate great influence of the type of the substituent, and hence a wide opportunity for fine-tuning and perspective for further development.

Scheme **1**. Synthetic routes for **SFX-PO-Br**-starting material and three studied emitters: **SFX-PO-DPA**, **SFX-PO-DPA-Me** and **SFX-PO-DPA-OMe**.

Crystal Structures

In order to gain further insights into these compounds, the structures of **SFX-PO-DPA** and **SFX-PO-DPA-Me** have been studied by single-crystal X-ray diffraction (Figure **S1**). The data obtained from X-ray diffraction analysis are summarized in Table **S1**. **SFX-PO-DPA** formed light-yellow rod-shaped crystals and was found to crystallize in the monoclinic space group *C2/c* when recrystallised from a mixture of methanol and dichloromethane by solvent layering. **SFX-PO-DPA-Me** formed pale-yellow block-shaped crystals in the monoclinic *I2/a* space group when recrystallised from a mixture of hexane and dichloromethane by evaporation. Recrystallization of **SFX-PO-DPA-Me** from the same mixture as for **SFX-PO-DPA** (i.e., methanol and dichloromethane by solvent layering) led to formation of pale-yellow block-shaped crystals in the same spaced group *C2/c*. The crystal structures and interactions between the materials and co-crystallized solvent molecules are shown in Figure **3**. As depicted in Figure **3**, co-crystallized solvent molecules have an influence on the dihedral angle between

fluorene and xanthene in the spiro-structure. When dichloromethane and hexane are present in the **SFX-PO-DPA-Me** molecule, the dihedral angle is 86.7°. However, switching to a more polar solvent system (dichloromethane and methanol), the angle increases to 89.5°. With the same solvent system (dichloromethane and methanol) applied to the crystallization of **SFX-PO-DPA** only two methanol molecules were incorporated in the structure leading to a dihedral angle of 87.6°. The variation in the value of the dihedral angle as a function of the environment will have an influence on through bond interactions between the orthogonally disposed donor and acceptor units, thereby affecting the photophysical properties of these spiro-based structures.
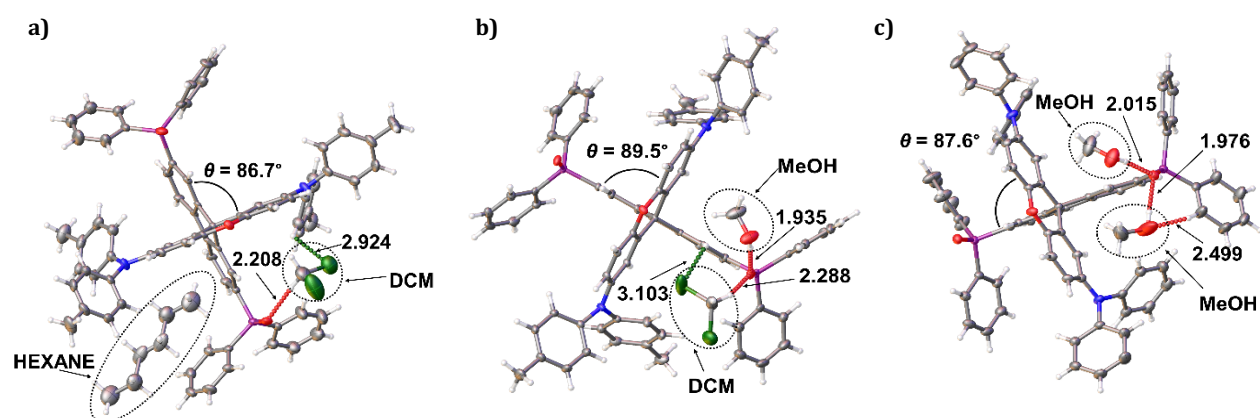
Figure **3**. Crystal structures and dihedral angles of (a) **SFX-PO-DPA-Me** recrystallized from DCM/Hexane, (b) **SFX-PO-DPA-Me** recrystallized from DCM/MeOH and (c) **SFX-PO-DPA** recrystallized from DCM:Hexane. Heteroatoms: O, red; N, blue; P, violet; Cl, green.

Electrochemical Properties.

The HOMO and LUMO energy levels of the three emitters were inferred from an analysis of the cyclic voltammetry (CV) and differential pulse voltammetry (DPV) measurements obtained in dichloromethane (for oxidation) and *N,N*-dimethylformamide (for reduction). The CVs and DPVs are shown in Figure **4** and the data are summarized in Table **1**. Each of the emitters exhibits two highly reversible oxidation waves, reflecting sequential oxidation of each of the two donor moieties. As predicted by the theoretical calculations (Figure **9**, *vide infra*), the HOMO in all three compounds is

delocalized across the two donor moieties through the xanthene bridge. Such delocalization can significantly stabilize the radical cation formed upon the first oxidation. As a result, removal of the second electron becomes less difficult than for a less-delocalized HOMO due in part to lower Coulombic repulsion and this is manifested in the fairly close spacing of the two CV oxidation waves.[29] For **SFX-PO-DPA**, $E_{ox,}$ the peak oxidation potential as determined from DPV, is 0.76 V. The oxidation potentials shifted cathodically with increasing donor strength to 0.73 V and 0.60 V for **SFX-PO-DPA-Me** and **SFX-PO-DPA-OMe**, respectively, consistent with the picture obtained by DFT calculations (Figure **9**, *vide infra*). These values are almost identical to the oxidation potentials of related tetrasubstituted hole transport materials, such as **SFX-MeOTAD** (0.52 V vs SCE) with four dimethoxydiphenylamine groups and **SFX-TAD** (0.68 V vs SCE) with four diphenylamine groups, reported by us previously.[26] This indicates no influence on the oxidation potential from the diphenylphosphine oxide-modified fluorene fragment. The HOMO energies were determined to be -5.56 eV, -5.53 eV and -5.40 eV for **SFX-PO-DPA**, **SFX-PO-DPA-Me** and **SFX-PO-DPA-OMe**, respectively. The decrease in HOMO energy is associated with the increase in mesomeric effect with increasing electron-donating strength of the amine donor groups. Only one irreversible reduction wave was observed for all three compounds. LUMO energies were inferred from the reduction potentials obtained by DPV measurements in DMF and were found to be -2.94 eV, -3.03 eV and -3.15 eV for **SFX-PO-DPA, SFX-PO-DPA-Me** and **SFX-PO-DPA-OMe**, respectively. Unexpectedly, we observed a small stabilization of the LUMO with increasing donor strength associated with an increase in stabilizing inductive effect by substituting DPA successively with Me and OMe substituents, whilst the mesomeric effect is negligible due to the complete localization of the LUMO on the acceptor (see molecular modelling section).
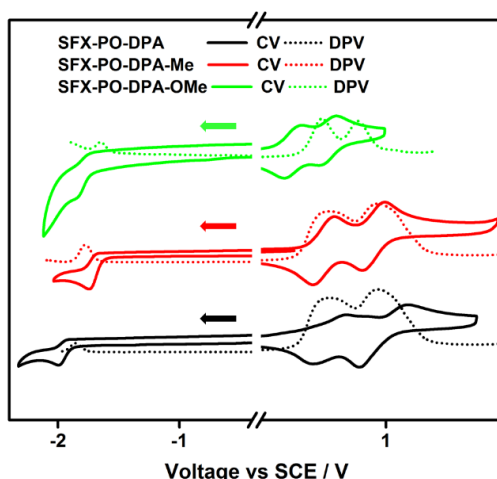
Figure **4**. Cyclic Voltammograms and Differential Pulse Voltammograms of **SFX-PO-DPA**, **SFX-PO-DPA-Me** and **SFX-PO-DPA-OMe** (Oxidation and reduction was performed in degassed DCM and DMF, respectively; scan rate: 100 mV s^{-1}).

Table **1**. Electrochemical properties of **SFX-PO-DPA**, **SFX-PO-DPA-Me** and **SFX-PO-DPA-OMe**.

	E_{ox} [a] / V	E_{red} [b] / V	HOMO [a,c] / eV	LUMO [b,c] / eV	ΔE_{redox} [d] / eV
SFX-PO-DPA	0.76	-1.86	-5.56	-2.94	2.62
SFX-PO-DPA-Me	0.73	-1.77	-5.53	-3.03	2.50
SFX-PO-DPA-OMe	0.60	-1.65	-5.40	-3.15	2.25

[a.] Oxidation peak obtained from DPV in DCM with 0.1 M [nBu$_4$N]PF$_6$ as the supporting electrolyte and Fc/Fc$^+$ as the internal reference and referenced ys SCE (Fc/Fc$^+$ = 0.46 V vs. SCE).[30] [b.] Reduction peak potential obtained from DPV in DMF with 0.1 M [nBu$_4$N]PF$_6$ as the supporting electrolyte and Fc/Fc$^+$ as the internal reference (0.45 V vs. SCE). [30] [c.] The HOMO and LUMO energies were determined using $E_{HOMO/LUMO} = -(E_{ox}/ E_{red} + 4.8)$ eV with potentials against Fc/Fc$^+$.[31] [d.] ΔE_{redox}= |E_{HOMO}-E_{LUMO}|.

Photophysical Properties.

Figure **5a** shows the UV-Vis absorption and photoluminescence (PL) spectra of the three emitters in toluene (PhMe) and the data are summarized in Table **2**. All three compounds exhibit similar optical absorption and possess a series of highly absorbing bands from 290 nm to 320 nm, which we attribute from Time-Dependent Density Functional Theory (TD-DFT) calculations to high-oscillator-strength locally excited electronic transitions to S$_n$ (n>1) states, while, as expected from its strong

charge-transfer character, the oscillator strength for the promotion to S_1 is much smaller (Tables **S4** and **5**, Figure **S14**). The PL spectra in degassed PhMe are broad and unstructured, typical of emission from a CT state. A red-shift in the emission from **SFX-PO-DPA** (λ_{PL} = 490 nm) to **SFX-PO-DPA-Me** (λ_{PL} = 492 nm) and to **SFX-PO-DPA-OMe** (λ_{PL} = 514 nm) is consistent with the decrease in the HOMO-LUMO gap, an observation corroborated by theoretical calculations (see Figure **9**, *vide infra*). The Φ_{PL} values of 56%, 80% and 68% for **SFX-PO-DPA**, **SFX-PO-DPA-Me** and **SFX-PO-DPA-OMe**, respectively, in degassed PhMe varied significantly as a function of the pendant groups on the donor amine. Emission was dramatically quenched, with much reduced Φ_{PL} of 19%, 38% and 25% **SFX-PO-DPA**, **SFX-PO-DPA-Me** and **SFX-PO-DPA-OMe**, respectively, upon exposure to air, an indication of triplet harvesting in the absence of oxygen.
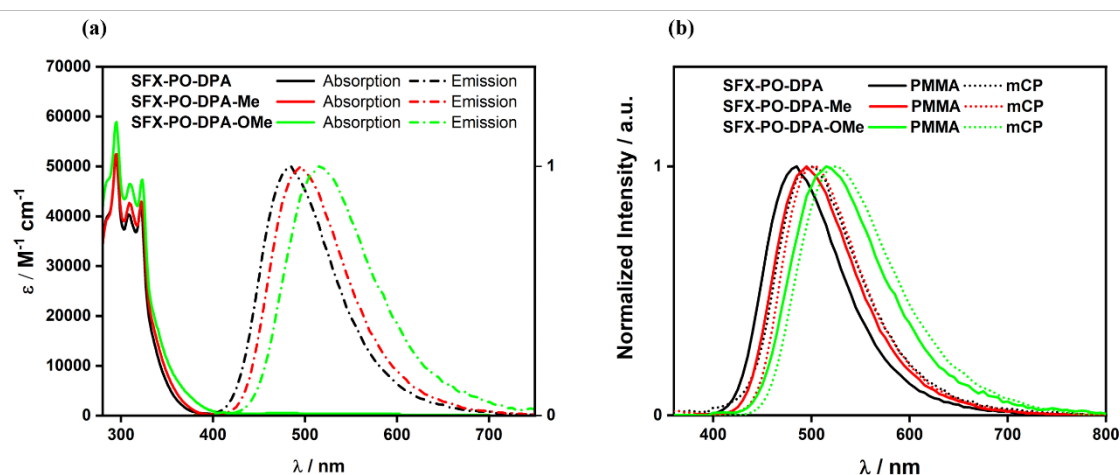
Figure **5**. (**a**) UV-Vis absorption and PL spectra in PhMe and (**b**) PL spectra in PMMA and mCP thin films of **SFX-PO-DPA** (10 wt% in both), **SFX-PO-DPA-Me** (10 wt% in PMMA and 15 wt% in mCP) and **SFX-PO-DPA-OMe** (10 wt% in both). λ_{exc} = 360 nm.

We next investigated the PL behavior of the three compounds in the solid state as doped films in both PMMA and mCP (Figure **5b**). Irrespective of the host, the emission profiles remained broad and unstructured. In solution-processed 10 wt% doped films in PMMA, all three compounds exhibited blue-green to green emission with λ_{PL} of 490 nm for **SFX-PO-DPA**, 495 nm for **SFX-PO-DPA-Me** and 515 nm for **SFX-PO-DPA-OMe**, results in line with those observed in toluene. However, the Φ_{PL} suffered

in the PMMA films and values of 10%, 38% and 25% were obtained for **SFX-PO-DPA**, **SFX-PO-DPA-Me** and **SFX-PO-DPA-OMe**, respectively. Time-resolved PL measurements in PMMA revealed bi-exponential decay profiles for all three emitters. **SFX-PO-DPA, SFX-PO-DPA-Me** and **SFX-PO-DPA-OMe** possessed prompt lifetimes, τ_p, of 92 ns, 126 ns and 156 ns, respectively, and delayed lifetimes, τ_d, of 10 μs, 9.4 μs and 6.4 μs, respectively. Based on the emission energies of the three emitters, mCP was chosen as the host matrix for OLEDs. Optimum doping concentrations of 10 wt% for **SFX-PO-DPA** and **SFX-PO-DPA-OMe**, and 15 wt% for **SFX-PO-DPA-Me** were determined based on a concentration-dependence study of absolute Φ_{PL} values of vacuum-deposited films (Table **S2**, ESI). At these concentrations, slightly red-shifted emission maxima of 500 nm for **SFX-PO-DPA** and **SFX-PO-DPA-Me**, and 520 nm for **SFX-PO-DPA-OMe** were observed along with much enhanced Φ_{PL} values of 50%, 70% and 58%, respectively, compared to the measurements in PMMA. Time-resolved PL measurements again showed bi-exponential decay behavior for all three emitters, with an enhanced contribution from the delayed emission (Figure **7**). In comparison to the non-polar host PMMA, faster transient PL dynamics were observed in mCP both in terms of prompt and delayed lifetimes. Prompt lifetimes of 81 ns (43%), 49 ns (18%) and 100 ns (40%), and delayed lifetimes of 8.4 μs (57%), 8.3 μs (82%) and 6.2 μs (60%) were obtained for **SFX-PO-DPA, SFX-PO-DPA-Me** and **SFX-PO-DPA-OMe**, respectively, showing that delayed fluorescence also occurs in the mCP host. The long radiative lifetimes measured for the prompt component of these compounds support the emission from CT states with limited overlap between hole and electron densities.
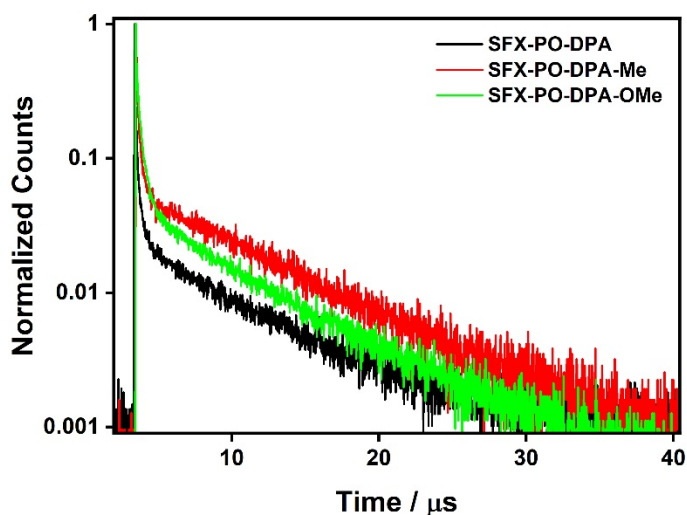
Figure **6**. Normalized time-resolved PL of vacuum-deposited mCP films with 10 wt% **SFX-PO-DPA**, 15 wt% **SFX-PO-DPA-Me** and 10 wt% **SFX-PO-DPA-OMe** at room temperature. λ_{exc} = 378 nm.

To further confirm the TADF character of these emitters, we next studied the temperature dependence of the time-resolved emission decays of the mCP doped films containing the three emitters. An increase in the relative intensity of the delayed component of the lifetime with increasing temperature provides direct evidence to support the TADF character of these spiro-based emitters (Figure **7a-c**). The ΔE_{ST} values in mCP of the three emitters were determined from the difference in the energies of the fluorescence and phosphorescence spectra obtained from the onset of prompt and delayed emission, respectively, at 77 K (Figure **9a-c**). Very small ΔE_{ST} values of 0.05 eV, 0.02 eV and 0.01 eV and S_1 energies of 2.85 eV, 2.80 eV and 2.75 eV were measured for **SFX-PO-DPA, SFX-PO-DPA-Me** and **SFX-PO-DPA-OMe** respectively, in line with theory (Table **S4**) and confirming their strong potential as efficient TADF emitters in the solid state.
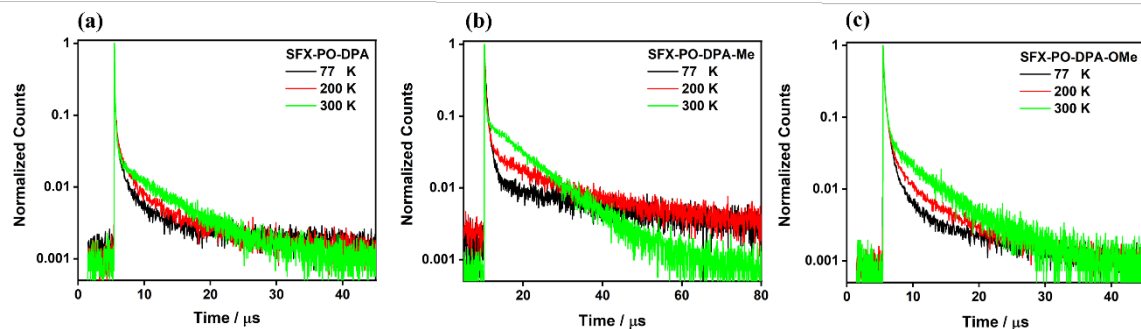
Figure **7**. Temperature-dependent time-resolved PL decay traces of doped films in mCP with (**a**) 10 wt% **SFX-PO-DPA** (**b**) 15 wt% **SFX-PO-DPA-Me** and (**c**) 10 wt% **SFX-PO-DPA-OMe** (λ_{exc} = 378 nm).

In order to understand the origin of the short τ_d and high Φ_{PL}, we calculated the rate constants for the radiative decay from the singlet state (k_r^S), RISC (k_{rISC}) and non-radiative decay from the triplet state (k_{nr}^T). It should be noted that the rate constants for radiative and non-radiative processes can only be explicitly calculated assuming a monoexponential decay of the emission. For bi-exponential decay, we calculated the corresponding rates making a set of assumptions as described previously (see ESI, section 5.2 for details).[32] All three emitters exhibited similar k_r^S on the order of 2.3-2.6 × 10^6 s^{-1} (Table **S3**). Importantly, k_{RISC}, which is a crucial parameter responsible for an efficient TADF mechanism, remained higher than the competing k_{nr}^T rate constant for all three emitters, implying that the thermal upconversion of excitons from T_1 to S_1 is preferred over non-radiative decay from the T_1 state. Furthermore, the relatively higher value of k_{RISC} coupled with a very small ΔE_{ST} in **SFX-PO-DPA-Me** is indicative of a faster and more efficient RISC mechanism in this emitter, which results in the highest Φ_{PL} values observed across all media. Such short τ_d values and large k_{RISC} have been shown to play a crucial role in realizing low efficiency roll-off in the devices by reducing the probability of triplet exciton quenching mechanisms.[33]
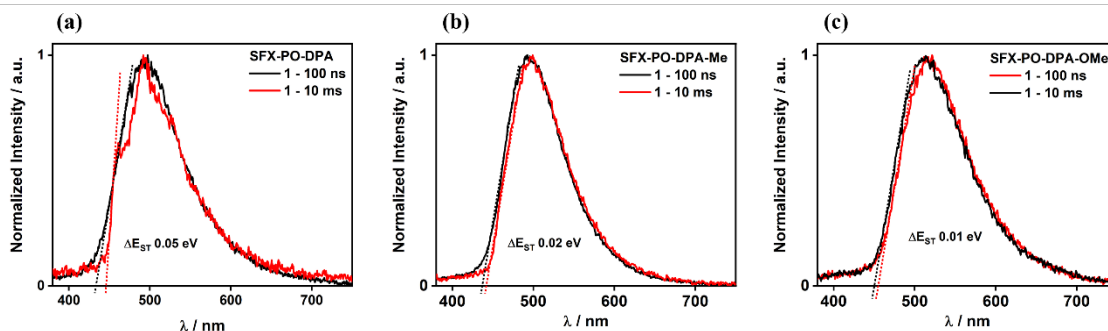
Figure **8.** Prompt and delayed (by 1 ms) spectra (at 77 K) of doped films in mCP with (**a**) 10 wt% **SFX-PO-DPA** (**b**) 15 wt% **SFX-PO-DPA-Me** and (**c**) 10 wt% **SFX-PO-DPA-OMe** (λ_{exc} = 355 nm).

Table **2**. Photophysical properties of **SFX-PO-DPA, SFX-PO-DPA-Me** and **SFX-PO-DPA-OMe**.

	λ_{abs}[a] / nm	λ_{PL}[a] / λ_{PL}[c] / nm	Φ_{PL}[b] / %	Φ_{PL}[c] / %	τ_p[c] / ns	τ_d[c] / μs	S_1 / T_1[d] / eV	ΔE_{ST}[d] / eV	k_{RISC}[e] / 10^5 s^{-1}	k_{nr}^{T}[e] / 10^4 s^{-1}
SFX-PO-DPA	290, 300, 320	490 / 500	56 (19)	50	49	8.4	2.85/2.80	0.05	2.64	7.53
SFX-PO-DPA-Me	290, 301,320	492 / 500	80 (38)	70	81	8.3	2.80/2.78	0.02	2.57	4.20
SFX-PO-DPA-OMe	290, 300, 320	514 / 520	68 (25)	58	100	6.2	2.75/2.74	0.01	2.32	8.79

[a] In PhMe at 298 K. [b] Quinine sulfate (0.5 M) in H_2SO_4 (aq) was used as the reference (Φ_{PL}: 54.6%, λ_{exc} =360 nm).[34] Values quoted are in degassed solutions, which were prepared by three freeze-pump-thaw cycles. Values in parentheses are for aerated solutions, which were prepared by bubbling air for 10 min. [c] Thin films were prepared by vacuum depositing 10 wt.% (15 wt.% for **SFX-PO-DPA-Me**) doped samples in mCP and values were determined using an integrating sphere (λ_{exc} = 340 nm); degassing was done by N_2 purge for 10 minutes. [d] Determined from the onset of the prompt and delayed emission spectra of 10 wt.% (15 wt.% for **SFX-PO-DPA-Me**) doped films in mCP, measured at 77 K (λ_{exc} = 355 nm). [e] In doped films in mCP matrix. See text for doping concentrations.

Molecular Modelling

Characterization of the electronic structure and optoelectronic properties of the three SFX spiro compounds has been carried on with the help of DFT calculations. More specifically, we used the methodology developed previously that offers a particularly accurate description of the electronic structure of materials for OLED applications (Figure **9**), namely the PBE0 functional was adopted and the excited-state properties calculated within the Tamm-Dancoff approximation.[35] The increasingly

shallower HOMO level along the series **SFX-PO-DPA, SFX-PO-DPA-Me** and **SFX-PO-DPA-OMe**

is consistent with the increasing donor strength of the diarylamine donor. For each emitter, the LUMO

is localized exclusively on the fluorene core with no contribution from the pendant phosphine oxides

and is only slightly affected by stabilizing inductive effects of the side groups attached to the **DPA** core.

S_1 energies decrease along the series from 2.77 eV for **SFX-PO-DPA** to 2.34 eV for **SFX-PO-DPA-**

OMe. Very small ΔE_{ST} values of 0.0038 eV for **SFX-PO-DPA** and **SFX-PO-DPA-Me** and 0.00051 eV

for **SFX-PO-DPA-OMe** reflect the near orthogonal arrangement of the donor and acceptor groups. We

determined the nature of the excited states using the Φ_S metric that quantifies the overlap between the

hole and electron densities as obtained in the attachment-detachment formalism (Figure **S15**, Table

S4).[36] Using this methodology, full charge-transfer (CT) [completely localized (LE)] excited states

feature $\Phi_S = 0$ [$\Phi_S = 1$] can be inferred. Φ_S values were calculated using the NANCY_EX package[37]

and the hole and the electron densities were visualised with DrawMol.[38] Very low values, $\Phi_S < 0.12$

(Table **S4**), were calculated for both the S_1 and T_1 states for all three emitters, implying excited states

with strong CT character. This is mirrored by the very small calculated oscillator strengths ranging from

0 to 10^{-4} and translates into radiative decay rates of $\sim 4.8 \times 10^4$ s^{-1} roughly two orders of magnitude

smaller than the experimental values (Table **S4**). A range of other functionals were applied to **SFX-PO-**

DPA-Me, with oscillator strength remaining very low (Table **S6**). Optimization of the singlet excited

state was also performed for **SFX-PO-DPA-Me** and offered a slight increase in the predicted oscillator

strength with a value of 2×10^{-4} resulting in a radiative rate of 9.7×10^4 s^{-1}, still much lower than the

experimental value.

The discrepancy between the theoretical and the experimental radiative decay rates for the

ground state and S_1 equilibrium geometries of **SFX-PO-DPA-Me** suggests that the Franck-Condon

approximation breaks down. Experimental and simulated emission are thus reconciled by invoking

Herzberg-Teller intensity borrowing, mediated via vibronic coupling. Within this framework,

perturbative interactions between the S_1 electronic wave function and nuclear motions result in a

combined electronic and vibronic state that can mix with nearby purely electronic states. We thus sum,

consistently with the Thomas-Kuhn-Reiche sum-rules, the oscillator strengths associated with each

vibronic transition from the ground state of vibration of state S_1 to the n-th vibrational levels of the ground state, S_0. Considering the undistorted-undisplaced harmonic oscillator approximation and the same energy for all vibronic transitions $\Delta E_{S_1 S_0}$ corresponding to the transition energy from the S_1 optimized geometry to the ground state, the oscillator strength for the transition between the S_1 and the ground states is (see Supporting Information for further details):

$$f^{S_1 S_0} = \sum_n \frac{2}{3} \frac{m_e}{e^2 \hbar^2} \Delta E_{S_1 S_0} \sum_{\alpha = x,y,z} [\langle S_1, 0 \mid \hat{\mu}_\alpha \mid S_0, n \rangle]^2$$

$$= \frac{2}{3} \frac{m_e}{e^2 \hbar^2} \Delta E_{S_1 S_0} \sum_{\alpha = x,y,z} [\mu_\alpha^{S_1 S_0, 0}]^2 + \frac{2}{3} \frac{m_e}{e^2 \hbar^2} \Delta E_{S_1 S_0} \sum_i \sum_{\alpha = x,y,z} \left[\left(\frac{\partial \mu_\alpha^{S_1 S_0}}{\partial Q_i} \right)_0 \sqrt{\frac{\hbar}{2\omega_i}} \right]^2$$

$$= f_0 + \sum_i f_i$$

Where m_e and e are the electron mass and charge, $\hbar$ is the reduced Planck constant, $\langle S_1, 0 \mid \hat{\mu}_\alpha \mid S_0, n \rangle$ is the transition dipole moment matrix element between the ground state of vibration of S_1 and the n-th vibrational level of S_0, $\mu_\alpha^{S_1 S_0, 0}$ is the $\alpha \equiv \{x, y, z\}$ component of the transition dipole moment computed at the S_1 optimized geometry, $\left(\frac{\partial \mu_\alpha^{S_1 S_0}}{\partial Q_i} \right)$ is the first derivative of the electronic transition dipole moment along the normal coordinates Q_i evaluated at the equilibrium geometry of the reference S_1 state, ω_i is the angular frequency of the ith normal mode; f_0 and f_i are the oscillator strengths computed at the S_1 optimized geometry and the Herzberg-Teller contribution of the i-th normal mode, respectively.
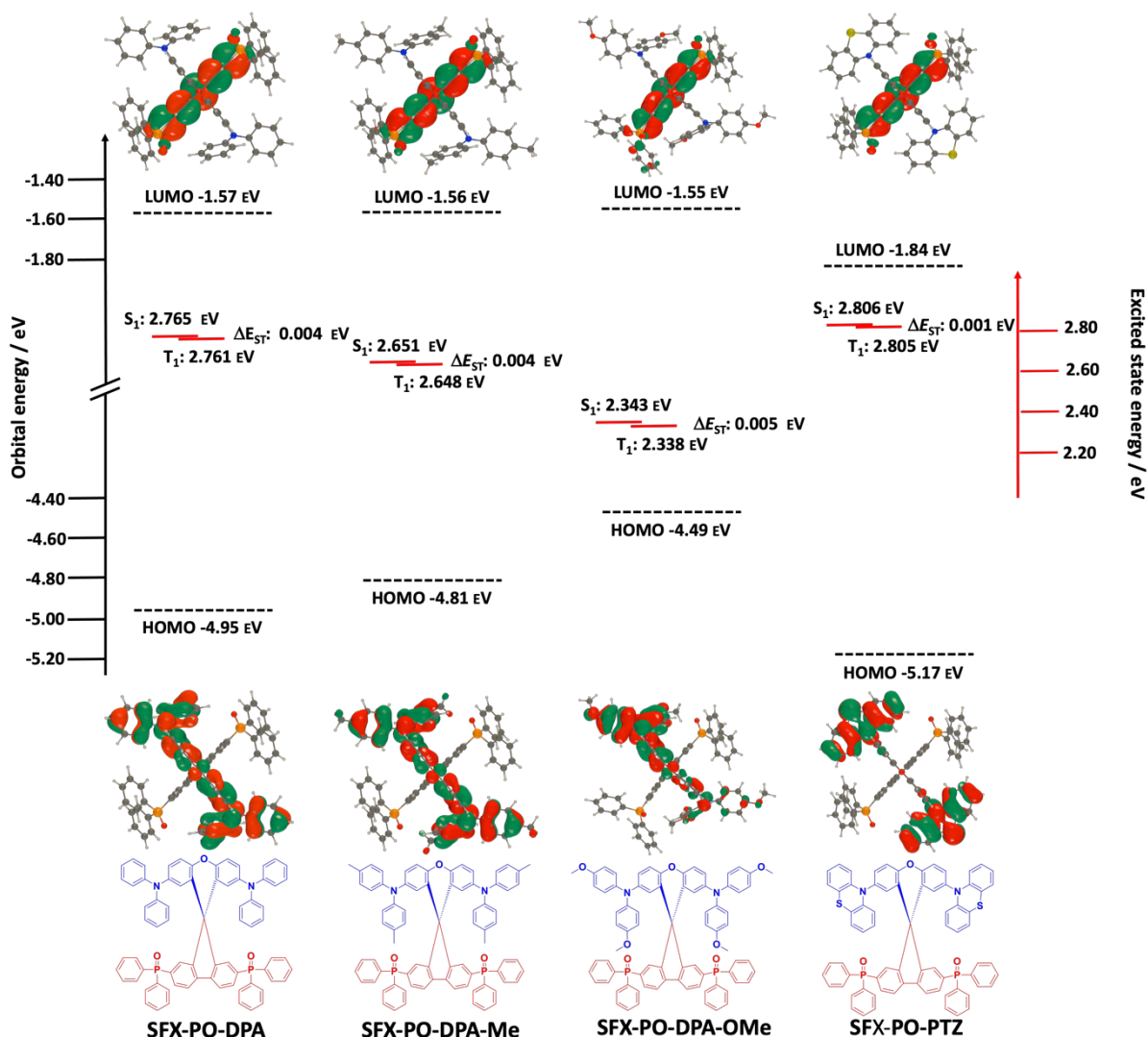
Figure **9**. Calculated HOMO, LUMO (as obtained at DFT PBE0 6-31G(d,p) level) S_1 and T_1 energies (as obtained at TDA-DFT PBE0 6-31G(d,p) level), and contour plots of the HOMO and LUMO orbitals of **SFX-PO-DPA, SFX-PO-DPA-Me**, **SFX-PO-DPA-OMe** and **SFX-PO-PTZ**.

In practice, the transition dipole moment derivative $\left(\frac{\partial \mu_\alpha^{S_1 S_0}}{\partial Q_i} \right)_0$ is obtained by displacing the S_1-optimized excited-state geometry along its normal modes by 0.01 Å $\sqrt{amu}$ in an interval going from -0.1 to 0.1 Å $\sqrt{amu}$ and fitting the transition dipole moment evolution as a function of the normal coordinate, Q_i, with a linear regression (see Table **S7**). To reduce computational cost, we selected vibrational modes leading to a concomitant bending of the electron-donating and electron-accepting

units, as these sensibly increase the hole and electron densities near the sp^3 hybridized carbon and therefore could prompt larger oscillator strength (Figure **10 S16**, Table **S8**). Accounting for these vibrations indeed results in an increase in oscillator strength up to 3.7×10^{-4}. This now brings the calculated radiative decay rate (considering a refractive index of 1.73 for mCP) to 1.81×10^5 s^{-1}, which is within the same order of magnitude as the measured value of $k_r = 2.3 \times 10^6$ s^{-1}, highlighting the importance of Herzberg-Teller effects in spiro-based compounds. We expect the (dynamic, i.e. induced by vibrations) increase in electron-hole overlap and in the ensuing radiative decay rate to be sensitive to the nature of the electron-active substituents. To verify this hypothesis, we designed compound **SFX-PO-PTZ**, where the **DPA-Me** side groups are replaced by stronger electron-donating phenothiazine (**PTZ**) groups, and carried out the same analysis, i.e., S$_1$ excited-state optimization followed by sampling along the relevant normal modes (Table **S9**). As expected, **SFX-PO-PTZ** exhibits an oscillator strength in the relaxed S$_1$ excited-state geometry that amounts to 7.13×10^{-5} when Herzberg-Teller corrections are included, which is one order of magnitude smaller than **SFX-PO-DPA-Me**. This result can be readily explained by the removal of the hole density away from the sp^3 carbon in presence of the stronger **PTZ** donor moieties (Figure **S17**, Table **S8**).
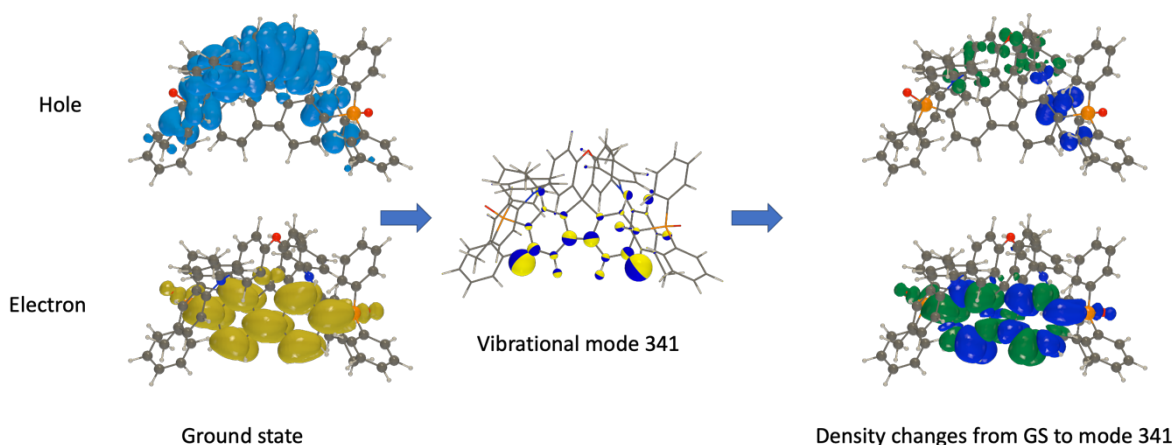

Figure **10**. Hole (h$^+$) electron (e$^-$) densities of **SFX-PO-DPA-OMe** for the undistorted (left panel) and distorted (right panel) S$_1$ along the vibrational mode at 1556.2 cm^{-1} (centre panel) leading to the largest enhancement in oscillator strength. The size and the orientation of the yellow and blue refer to the

amplitude and the displacement vector, respectively. Difference hole and electron densities between the distorted (0.1 Å $\sqrt{amu}$) and the undistorted geometry with the green color for positive lobes and blue for negative ones (right panel). The isovalue for the hole and electron densities amounts to 4×10^{-4} while for the difference hole and electron densities, it amounts to 4×10^{5}.

Device Fabrication.

The photophysical picture points to spiro-based compounds that are TADF emitters and have high Φ_{PL} in mCP and short τ_d. These compounds were therefore assessed as emitters in OLEDs. The OLED device stack architecture is shown in Figure **11** and consists of: ITO / NPB (30 nm) / TCTA (20 nm) / mCP (10 nm) / Emitter: mCP (20 nm) / DPEPO (10 nm) / TmPyPB (40 nm) / LiF (1 nm) / Al (100 nm), where *N,N'*-bis(naphthalen-1-yl)-*N,N'*-bis(phenyl)benzidine (NPB) was used as a hole injection layer (HIL), tris(4-carbazoyl-9-ylphenyl)amine (TCTA) was used as a hole transporting layer (HTL), mCP (1,3-bis(*N*-carbazolyl)benzene) and DPEPO were used as an electron and hole blockers, respectively. 1,3,5-tris(3-pyridyl-3-phenyl)benzene (TmPyPB) was chosen as the electron transporting layer (ETL) as it possesses a high electron mobility of 10^{-4} cm^2 V^{-1} s^{-1} and a high triplet energy of 2.75 eV along with a deep HOMO energy of 6.7 eV.[39] The emissive layer (EML) consisted of 10 wt% doped films of **SFX-PO-DPA**, **SFX-PO-DPA-OMe** and 15 wt% doped film of **SFX-PO-DPA-Me** in mCP.
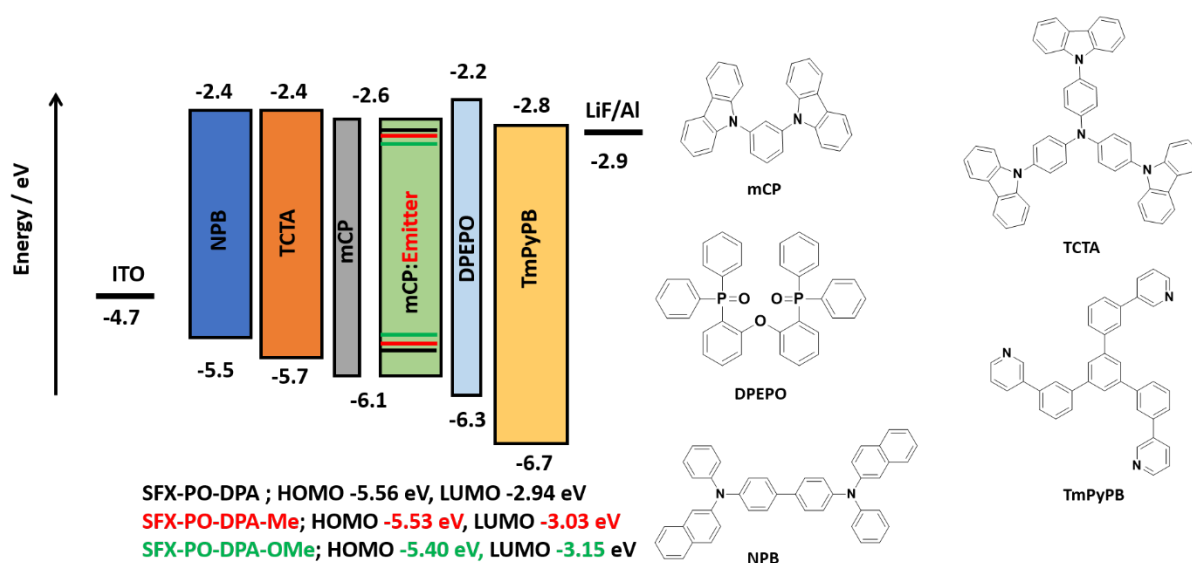

Figure **11**. Chemical structures and energy levels of materials used for device fabrication.

The electroluminescence properties are shown in Figure **12** and data are summarized in Table **3**. The three emitters exhibited blue-green to green electroluminescence with systematic red-shifting of the EL spectra as a function of donor strength, in parallel to the trends and maxima observed in their respective PL spectra. The OLED with **SFX-PO-DPA** showed a λ_{EL} of 500 nm with CIE coordinates of (0.20, 0.47), the OLED with **SFX-PO-DPA-Me** showed a slight red-shift with a λ_{EL} of 502 nm and CIE coordinates of (0.23, 0.50) and **SFX-PO-DPA-OMe** displayed the most red-shifted EL spectrum with a λ_{EL} of 520 nm and CIE coordinates of (0.29, 0.56). All OLEDs showed steep current-voltage-luminance behavior (Figures **12a** and **12b**) with low turn-on voltages of 3.2 V for devices within **SFX-PO-DPA** and **SFX-PO-DPA-Me** and 3.8 V for the device with **SFX-PO-DPA-OMe**.
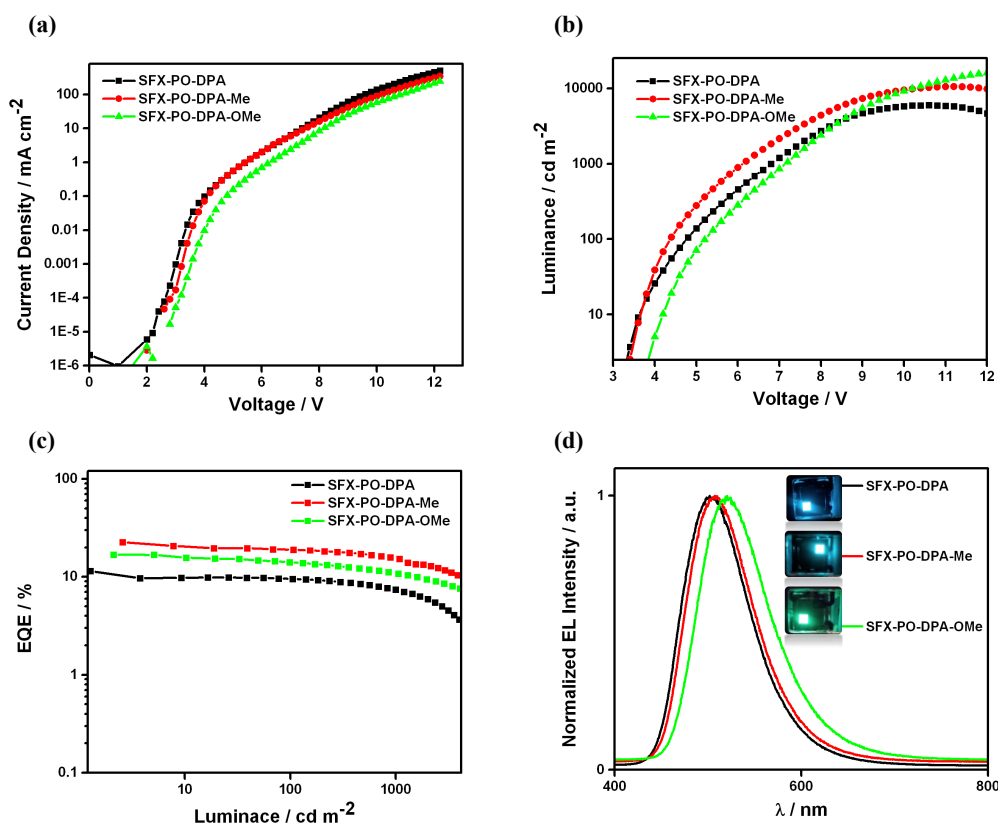

Figure **12** (**a**) Current density-voltage characteristics (**b**) Luminance vs Voltage. (**c**) EQE vs Luminance (**d**) Normalized EL spectra of **SFX-PO-DPA** (black), **SFX-PO-DPA-Me** (red) and **SFX-PO-DPA-OMe** (green).

Figure **12c** shows the EQE vs luminance behavior of the three devices. The OLED with **SFX-PO-DPA-Me** showed an excellent device performance with an EQE_{max} of 23% at a brightness of 2.5 cd m^{-2} and relatively low roll-off, with an EQE_{100} of 19% at a display-relevant brightness of 100 cd m^{-2}. Similarly, the OLEDs with **SFX-PO-DPA** and **SFX-PO-DPA-OMe** also maintained high EQE_{max} values of 11% and 16%, respectively, at low luminance, and likewise showed low efficiency roll-off with EQE_{100} of 9% and 15%, respectively. Even at a luminance of 1000 cd m^{-2}, EQE_{1000} of 7%, 16% and 12% were maintained for the OLEDs with **SFX-PO-DPA**, **SFX-PO-DPA-Me** and **SFX-PO-DPA-OMe**, respectively. The high observed EQEs are indicative of efficient triplet harvesting while the low efficiency roll-offs are due to the short τ_d values, which are beneficial in reducing the various triplet exciton quenching mechanisms such as triplet-triplet annihilation (TTA) and triplet polaron annihilation (TPA) in the devices. The poorer device performance of the OLEDs with **SFX-PO-DPA** and **SFX-PO-DPA-OMe** can be correlated to their lower Φ_{PL} values (Table **1**). Compared to the reported OLEDs with spiro-based emitters shown in Figure **1**, the devices based on **SFX-PO-DPA-Me** show the best performance in terms of EQE_{max} and reduced efficiency roll-off. Further, **SFX-PO-DPA** and **SFX-PO-DPA-OMe** emitters show comparable EQE_{max} values and improved efficiency roll-off characteristics compared to literature devices.

Table **3**. Electroluminescence Properties of **SFX-PO-DPA, SFX-PO-DPA-Me and SFX-PO-DPA-OMe.**

	V_{on} [a] / V	λ_{EL} [b] / nm	EQE_{max} [c]; EQE_{100} [d]; EQE_{1000} [e] / %	CE_{max} [c] / cd A^{-1}	PE_{max} [c] / lm W^{-1}	CIE [f] / (x,y)
SFX-PO-DPA	3.2	490	11; 9; 7	30.6	29.7	(0.21, 0.47)
SFX-PO-DPA-Me	3.2	500	23; 19; 16	62.8	58.1	(0.23, 0.50)
SFX-PO-DPA-OMe	3.8	520	16; 14; 12	53.1	43.9	(0.29, 0.56)

[a.] Measured at 1 cd/m^2. [b.] Emission maximum at 1 mA/cm^2. [c.] Maximum efficiencies at 1 cd/m^2. [d.] EQE at 100 cd/m^2. [e.] EQE at 1000 cd/m^2. [f.] Commission Internationale de l'Éclairage coordinates at 1 mA/cm^2.

Conclusions.

We have successfully synthesized a series of spiro-configured xanthene-based TADF emitters, which exhibit a confluence of desirable photophysical properties. We have demonstrated an efficient synthetic strategy to incorporate **SFX** bridge to realize highly sterically demanding structures that translate into materials that possess short delayed lifetimes of < 10 μs, very small ΔE_{ST} values coupled with high Φ_{PL} in the solid state. Molecular modelling reveals that the emission in these compounds occurs through a Herzberg-Teller mechanism where some intramolecular vibrations promote larger overlapping electron and hole density in vicinity of the sp^3 carbon atoms, thereby enhancing the radiative decay rate. The designed compounds exhibit non-radiative decay rates an order of magnitude slower than the rate of reverse intersystem crossing. The resulting OLEDs exhibited EQE_{max} values as high as 23% and with only modest efficiency roll-off at 100 and 1000 cd m^{-2} as a result of the short delayed lifetimes and reduced triplet-triplet and triplet-polaron annihilation associated with the expected reduced triplet diffusion due to the bulky shape of our compounds. These results clearly illustrated how crucial an **SFX** blocking unit is in realizing highly efficient TADF systems, which we believe will reinvigorate the importance of spiro system in TADF community.

Supporting Information

Synthesis protocols, NMR spectra, crystallographic data, supplementary photophysical measurements, computational data obtained from DFT and TD DFT and electroluminescence data.

Acknowledgements

References

(1) Yang, Z.; Mao, Z.; Xie, Z.; Zhang, Y.; Liu, S.; Zhao, J.; Xu, J.; Chi, Z.; Aldred, M. P., Recent advances in organic thermally activated delayed fluorescence materials. *Chem. Soc. Rev.* **2017**, *46*, 915-1016.
(2) Liu, Y.; Li, C.; Ren, Z.; Yan, S.; Bryce, M. R., All-organic thermally activated delayed fluorescence materials for organic light-emitting diodes. *Nat. Rev. Mater.* **2018**, *3*, 18020.
(3) Wong, M. Y.; Zysman-Colman, E., Purely Organic Thermally Activated Delayed Fluorescence Materials for Organic Light-Emitting Diodes. *Adv Mater* **2017**, *29*, 1605444.
(4) Cai, X.; Su, S.-J., Marching Toward Highly Efficient, Pure-Blue, and Stable Thermally Activated Delayed Fluorescent Organic Light-Emitting Diodes. *Adv. Funct. Mater.* **2018**, *28*.
(5) Zhang, Q.; Li, B.; Huang, S.; Nomura, H.; Tanaka, H.; Adachi, C., Efficient blue organic light-emitting diodes employing thermally activated delayed fluorescence. *Nat. Photonics* **2014**, *8*, 326-332.
(6) Hirata, S.; Sakai, Y.; Masui, K.; Tanaka, H.; Lee, S. Y.; Nomura, H.; Nakamura, N.; Yasumatsu, M.; Nakanotani, H.; Zhang, Q.; Shizu, K.; Miyazaki, H.; Adachi, C., Highly efficient blue electroluminescence based on thermally activated delayed fluorescence. *Nat Mater* **2015**, *14*, 330-336.
(7) Kim, G. H.; Lampande, R.; Im, J. B.; Lee, J. M.; Lee, J. Y.; Kwon, J. H., Controlling the exciton lifetime of blue thermally activated delayed fluorescence emitters using a heteroatom-containing pyridoindole donor moiety. *Materials Horizons* **2017**, *4*, 619-624.
(8) Sun, J. W.; Baek, J. Y.; Kim, K.-H.; Moon, C.-K.; Lee, J.-H.; Kwon, S.-K.; Kim, Y.-H.; Kim, J.-J., Thermally Activated Delayed Fluorescence from Azasiline Based Intramolecular Charge-Transfer Emitter (DTPDDA) and a Highly Efficient Blue Light Emitting Diode. *Chem. Mater.* **2015**, *27*, 6675-6681.
(9) Lin, T.-A.; Chatterjee, T.; Tsai, W.-L.; Lee, W.-K.; Wu, M.-J.; Jiao, M.; Pan, K.-C.; Yi, C.-L.; Chung, C.-L.; Wong, K.-T.; Wu, C.-C., Sky-Blue Organic Light Emitting Diode with 37% External Quantum Efficiency Using Thermally Activated Delayed Fluorescence from Spiroacridine-Triazine Hybrid. *Adv. Mater.* **2016**, *28*, 6976-6983.
(10) Saragi, T. P. I.; Spehr, T.; Siebert, A.; Fuhrmann-Lieker, T.; Salbeck, J., Spiro Compounds for Organic Optoelectronics. *Chem. Rev.* **2007**, *107*, 1011-1065.
(11) Luo, J.; Zhou, Y.; Niu, Z.-Q.; Zhou, Q.-F.; Ma, Y.; Pei, J., Three-Dimensional Architectures for Highly Stable Pure Blue Emission. *J. Am. Chem. Soc.* **2007**, *129*, 11314-11315.
(12) Gu, J.-F.; Xie, G.-H.; Zhang, L.; Chen, S.-F.; Lin, Z.-Q.; Zhang, Z.-S.; Zhao, J.-F.; Xie, L.-H.; Tang, C.; Zhao, Y.; Liu, S.-Y.; Huang, W., Dumbbell-Shaped Spirocyclic Aromatic Hydrocarbon to Control

Intermolecular π–π Stacking Interaction for High-Performance Nondoped Deep-Blue Organic Light-Emitting Devices. *The Journal of Physical Chemistry Letters* **2010**, *1*, 2849-2853.

(13) Seo, J.-A.; Gong, M. S.; Lee, J. Y., Thermally stable indoloacridine type host material for high efficiency blue phosphorescent organic light-emitting diodes. *Org. Electron.* **2014**, *15*, 3773-3779.

(14) Poriel, C.; Sicard, L.; Rault-Berthelot, J., New generations of spirobifluorene regioisomers for organic electronics: tuning electronic properties with the substitution pattern. *Chem. Commun.* **2019**, *55*, 14238-14254.

(15) Lucas, F.; Ibraikulov, O. A.; Quinton, C.; Sicard, L.; Heiser, T.; Tondelier, D.; Geffroy, B.; Leclerc, N.; Rault-Berthelot, J.; Poriel, C., Spirophenylacridine-2,7-(diphenylphosphineoxide)-fluorene: A Bipolar Host for High-Efficiency Single-Layer Blue Phosphorescent Organic Light-Emitting Diodes. *Adv. Optical Mater.* **2020**, *8*, 1901225.

(16) Nakagawa, T.; Ku, S. Y.; Wong, K. T.; Adachi, C., Electroluminescence based on thermally activated delayed fluorescence generated by a spirobifluorene donor-acceptor structure. *Chem. Commun.* **2012**, *48*, 9580-9582.

(17) Mehes, G.; Nomura, H.; Zhang, Q.; Nakagawa, T.; Adachi, C., Enhanced electroluminescence efficiency in a spiro-acridine derivative through thermally activated delayed fluorescence. *Angew Chem Int Ed Engl* **2012**, *51*, 11311-11315.

(18) Nasu, K.; Nakagawa, T.; Nomura, H.; Lin, C. J.; Cheng, C. H.; Tseng, M. R.; Yasuda, T.; Adachi, C., A highly luminescent spiro-anthracenone-based organic light-emitting diode exhibiting thermally activated delayed fluorescence. *Chem. Commun.* **2013**, *49*, 10385-10387.

(19) Ohkuma, H.; Nakagawa, T.; Shizu, K.; Yasuda, T.; Adachi, C., Thermally Activated Delayed Fluorescence from a Spiro-diazafluorene Derivative. *Chem. Lett.* **2014**, *43*, 1017-1019.

(20) Wang, Y.-K.; Wu, S.-F.; Yuan, Y.; Li, S.-H.; Fung, M.-K.; Liao, L.-S.; Jiang, Z.-Q., Donor−σ−Acceptor Molecules for Green Thermally Activated Delayed Fluorescence by Spatially Approaching Spiro Conformation. *Org. Lett.* **2017**, *19*, 3155-3158.

(21) Rao, J.; Zhao, C.; Wang, Y.; Bai, K.; Wang, S.; Ding, J.; Wang, L., Achieving Deep-Blue Thermally Activated Delayed Fluorescence in Nondoped Organic Light-Emitting Diodes through a Spiro-Blocking Strategy. *ACS Omega* **2019**, *4*, 1861-1867.

(22) Zhu, X.-D.; Peng, C.-C.; Kong, F.-C.; Yang, S.-Y.; Li, H.-C.; Kumar, S.; Wang, T.-T.; Jiang, Z.-Q.; Liao, L.-S., Acceptor modulation for improving a spiro-type thermally activated delayed fluorescence emitter. *J. Mater. Chem. C* **2020**, *8*, 8579-8584.

(23) Wang, Y.-K.; Huang, C.-C.; Ye, H.; Zhong, C.; Khan, A.; Yang, S.-Y.; Fung, M.-K.; Jiang, Z.-Q.; Adachi, C.; Liao, L.-S., Through Space Charge Transfer for Efficient Sky-Blue Thermally Activated Delayed Fluorescence (TADF) Emitter with Unconjugated Connection. *Adv. Optical Mater.* **2020**, *8*, 1901150.

(24) Poriel, C.; Cocherel, N.; Rault-Berthelot, J.; Vignau, L.; Jeannin, O., Incorporation of spiroxanthene units in blue-emitting oligophenylene frameworks: a new molecular design for OLED applications. *Chemistry* **2011**, *17*, 12631-12645.

(25) Xie, L.-H.; Liu, F.; Tang, C.; Hou, X.-Y.; Hua, Y.-R.; Fan, Q.-L.; Huang, W., Unexpected One-Pot Method to Synthesize Spiro[fluorene-9,9'-xanthene] Building Blocks for Blue-Light-Emitting Materials. *Org. Lett.* **2006**, *8*, 2787-2790.

(26) Maciejczyk, M.; Ivaturi, A.; Robertson, N., SFX as a low-cost 'Spiro' hole-transport material for efficient perovskite solar cells. *J. Mater. Chem. A* **2016**, *4*, 4855-4863.

(27) Zhao, J.; Xie, G.-H.; Yin, C.-R.; Xie, L.-H.; Han, C.-M.; Chen, R.-F.; Xu, H.; Yi, M.-D.; Deng, Z.-P.; Chen, S.-F.; Zhao, Y.; Liu, S.-Y.; Huang, W., Harmonizing Triplet Level and Ambipolar Characteristics of Wide-Gap Phosphine Oxide Hosts toward Highly Efficient and Low Driving Voltage Blue and Green PHOLEDs: An Effective Strategy Based on Spiro-Systems. *Chem. Mater.* **2011**, *23*, 5331-5339.

(28) Sadighi, J. P.; Harris, M. C.; Buchwald, S. L., A highly active palladium catalyst system for the arylation of anilines. *Tetrahedron Lett.* **1998**, *39*, 5327-5330.

(29) Fungo, F.; Wong, K.-T.; Ku, S.-Y.; Hung, Y.-Y.; Bard, A. J., Electrogenerated Chemiluminescence. 81. Influence of Donor and Acceptor Substituents on the ECL of a Spirobifluorene-Bridged Bipolar System. *J. Phys. Chem. B* **2005**, *109*, 3984-3989.

(30) Connelly, N. G.; Geiger, W. E., Chemical Redox Agents for Organometallic Chemistry. *Chem. Rev.* **1996**, *96*, 877-910.

(31) Cardona, C. M.; Li, W.; Kaifer, A. E.; Stockdale, D.; Bazan, G. C., Electrochemical Considerations for Determining Absolute Frontier Orbital Energy Levels of Conjugated Polymers for Solar Cell Applications. *Adv. Mater.* **2011**, *23*, 2367-2371.

(32) Masui, K.; Nakanotani, H.; Adachi, C., Analysis of exciton annihilation in high-efficiency sky-blue organic light-emitting diodes with thermally activated delayed fluorescence. *Org. Electron.* **2013**, *14*, 2721-2726.

(33) Chen, Z.; Wu, Z.; Ni, F.; Zhong, C.; Zeng, W.; Wei, D.; An, K.; Ma, D.; Yang, C., Emitters with a pyridine-3,5-dicarbonitrile core and short delayed fluorescence lifetimes of about 1.5 µs: orange-red TADF-based OLEDs with very slow efficiency roll-offs at high luminance. *J. Mater. Chem. C* **2018**, *6*, 6543-6548.

(34) Melhuish, W. H., Quantum Efficiences Of Fluorescence Of Organic Substances: Effect Of Solvent And Concentration Of The Fluorescent Solute 1. *J. Phys. Chem.* **1961**, *65*, 229-235.

(35) Moral, M.; Muccioli, L.; Son, W. J.; Olivier, Y.; Sancho-García, J. C., Theoretical Rationalization of the Singlet–Triplet Gap in OLEDs Materials: Impact of Charge-Transfer Character. *J. Chem. Theory Comput.* **2015**, *11*, 168-177.

(36) Olivier, Y.; Moral, M.; Muccioli, L.; Sancho-García, J.-C., Dynamic nature of excited states of donor–acceptor TADF materials for OLEDs: how theory can reveal structure–property relationships. *J. Mater. Chem. C* **2017**, *5*, 5718-5729.

(37) Etienne, T.; Assfeld, X.; Monari, A., Toward a Quantitative Assessment of Electronic Transitions' Charge-Transfer Character. *J. Chem. Theory Comput.* **2014**, *10*, 3896-3905.

(38) V. Liégeois, DrawMol, UNamur, https://www.unamur.be/drawmol, 2021.

(39) Su, S.-J.; Chiba, T.; Takeda, T.; Kido, J., Pyridine-Containing Triphenylbenzene Derivatives with High Electron Mobility for Highly Efficient Phosphorescent OLEDs. *Adv. Mater.* **2008**, *20*, 2125-2130.

(40) Grisanti, L.; Olivier, Y.; Wang, L.; Athanasopoulos, S.; Cornil, J.; Beljonne, D., Roles of local and nonlocal electron-phonon couplings in triplet exciton diffusion in the anthracene crystal. *Physical Review B* **2013**, *88*, 035450.

TOC graphic